International Journal of Fatigue 82 (2016) 332–341

Contents lists available at ScienceDirect

International Journal of Fatigue

journal homepage: www.elsevier.com/locate/ijfatigue

Mitigating time-dependent crack growth in Ni-base superalloy components

Kwai S. Chan [a,*], Michael P. Enright [a], Jonathan Moody [a], Simeon H.K. Fitch [b]

[a] Southwest Research Institute, San Antonio, TX 78238, USA
[b] Elder Research Inc., Charlottesville, VA 22903, USA

ARTICLE INFO

Article history:
Received 21 October 2014
Received in revised form 27 February 2015
Accepted 25 March 2015
Available online 2 April 2015

Keywords:
Time-dependent crack growth
Dwell fatigue
Small-scale creep
Life-prediction
Risk mitigation

ABSTRACT

Advanced Ni-based gas turbine disks are expected to operate at higher service temperatures in aggressive environments for longer time durations. Exposures of Ni-base alloys to these aggressive environments can lead to cycle-dependent and time-dependent crack growth in superalloy components for advanced turbopropulsion systems. In this article, the effects of tertiary γ' on the crack-tip stress relaxation process, oxide fracture and time-dependent crack growth kinetics are treated in a micromechanical model which is then incorporated into the DARWIN® probabilistic life-prediction code. Using the enhanced risk analysis tool and material constants calibrated to powder-metallurgy (PM) disk alloy ME3, the effects of grain size and tertiary γ' size on combined *time-dependent* and *cycle-dependent* crack growth in a PM Ni-alloy disk is demonstrated for a generic rotor design and a realistic mission profile using DARWIN. The results of this investigation are utilized to assess the effects of controlling grain size and γ' size on the risk of disk fracture and to identify possible means for mitigating time-dependent crack growth (TDCG) in hot-section components.

1. Introduction

Hot-section components in advanced turbopropulsion systems are expected to operate at higher heat dwell conditions for longer time durations than those in current service conditions. Under high heat dwell environments, advanced Ni-base superalloys intended for engine disk applications may be susceptible to concurrent time-dependent damage modes such as oxidation, stress corrosion, and creep in additional to cycle-dependent fatigue crack initiation and growth, which often manifest synergetic interaction effects on crack growth rates. Current life-prediction methodologies, however, generally do not treat synergetic interactions of multiple damage modes on component life reliability. Thus, there is a need to develop a probabilistic time-dependent fracture mechanics analysis capability for treating multiple damage modes in advanced Ni-based alloys for operations with long duration at high temperatures where time-dependent degradation mechanisms such as creep, oxidation, corrosion, and stress rupture may compete with time-independent fatigue crack growth as the component life-limiting mechanism [1,2]. On the other hand, advanced processing techniques and heat-treatment procedures have also been developed to create tailored microstructures in gas turbine disks. It is now possible to fabricate powder-metallurgy turboengine disks with controlled grain size and gamma prime sizes in the bore, rim, and transition zone of advanced Ni-base superalloys such as LSHR [3–5]. These advances in processing and heat-treatment techniques provide a new avenue for designing local microstructures with location-specific properties to combat and mitigate cycle-dependent and time-dependent crack growth mechanisms that are operative at high-dwell environments through an integrated computational design, processing, life-prediction, and risk assessment route.

This article focuses on the development of a fracture mechanics life-prediction methodology that can be utilized in two ways: (1) to treat multiple damage mechanisms pertinent for high-heat dwell environments in turboengine systems, and (2) to serve as a life-prediction and risk assessment tool in an integrated computational design and manufacturing platform [1,2]. To achieve this ultimate objective, a generic fracture mechanics approach has been implemented in a probabilistic life-prediction code, DARWIN [6], to treat the interaction of cycle-based and time-based crack growth resulting from various fatigue and fracture mechanisms, including those involving environmental degradation mechanisms such as oxidation, corrosion, stress rupture and creep. In this approach, cycle-dependent fatigue crack growth and time-dependent crack growth are treated as two independent processes

* Corresponding author.
E-mail address: kchan@swri.org (K.S. Chan).

http://dx.doi.org/10.1016/j.ijfatigue.2015.03.020
0142-1123/

whose crack growth increment, da, over a mission can be summed according to the expression given by [7–9]

$$(da)_{mission} = \left(\frac{da}{dN}\right)_{cyclic} dN + \left(\frac{da}{dt}\right) dt \quad (1)$$

where the first term on the right-hand-side of Eq. (1) treats cycle-dependent crack growth while the second term treats time-dependent crack growth for an arbitrary loading history within a mission. For fatigue crack growth test data generated under a constant frequency with dwell (as in dwell fatigue tests), Eq. (1) can be expressed as [7–9]

$$\left(\frac{da}{dN}\right)_{dwell} = \left(\frac{da}{dN}\right)_{cyclic} + \left[t_d + \frac{1}{f}\right]\left(\frac{da}{dt}\right) \quad (2)$$

where t_d is the dwell time and f is the frequency of the dwell fatigue cycles. To obtain the crack growth life, Eq. (2) is integrated over the fatigue cycle. The fatigue crack growth rate, da/dN, can be represented in terms of the Paris power-law [10] or a microstructure-based version [11], as given by

$$\frac{da}{dN} = A\Delta K^n \quad \text{for } \Delta K > \Delta K_{th} \quad (3)$$

where ΔK is the stress intensity range, ΔK_{th} is the large-crack crack growth threshold, and A and n are material constants. Cyclic crack growth generally follows a transgranular path, while time-dependent crack growth due to stress-assisted grain boundary oxidation typically follows an intergranular path [12–16]. The transition from transgranular fracture to intergranular fracture depends on the temperature, load frequency, and hold time. In general, time-dependent crack growth under K-controlled conditions can be expressed as [9,17,18]

$$\frac{da}{dt} = B_o \exp\left(-\frac{Q}{RT}\right) K^m \quad \text{with } m > 0 \text{ and } K > K_{th} \quad (4)$$

where K_{th} is the static crack growth threshold and B_o is a material constant which can be determined empirically from experimental data or evaluated from micromechanical models that relate B_o to material parameters. Both types of time-dependent crack growth models have been developed and reported in earlier publications [9,17]. For oxidation-induced crack growth, da/dt is described by [17]

$$\frac{da}{dt} = \frac{s_o}{t_o}\left(\frac{\pi E}{2\sigma_y \varepsilon_f^*}\right)^{m/2}\left(\frac{1}{E\sqrt{\pi d_o}}\right)^{m}\left(\frac{D_o}{D}\right)^{m\gamma/2} \times \exp\left(-\frac{Q}{RT}\right) K^m \quad \text{with } m > 0 \text{ and } K > K_{th} \quad (5)$$

where E is Young's modulus, σ_y is the yield stress, s_o is the reference penetration distance, t_o is the reference time, d_o is the reference crack-tip element size, D_o is the reference grain size, D is the grain size, m is the crack growth exponent, Q is the activation energy, R is the universal gas constant, T is the absolute temperature, and γ is the grain size exponent. Eq. (5) can be expressed in the form of Eq. (4) with B_o serving as a material constant that incorporates all material-related parameters. For the microstructure-based model, the material constant B_o is given by [17]

$$B_o = \frac{s_o}{t_o}\left(\frac{\pi E}{2\sigma_y \varepsilon_f^*}\right)^{m/2}\left(\frac{1}{E\sqrt{\pi d_o}}\right)^{m}\left(\frac{D_o}{D}\right)^{m\gamma/2} \quad (6)$$

which depends on the underlying microstructure but not on the temperature, stress or the stress intensity factor, K. Details of the derivation for Eq. (5) including a validation of the grain size dependence can be found in a recent publication [17].

The objective of this article is to report the development of a time-dependent crack growth for treating the effects of creep stress relaxation at the crack tip on time-dependent crack growth in Ni-based superalloys. The micromechanical crack growth model is then implemented into DARWIN [3] and the methodology is utilized to perform life-prediction and risk assessment for a fictitious engine disk made from a powder metallurgy alloy ME3, also referred to as Rene 104, with a designed microstructure of controlled grain size and tertiary gamma size. The development of the time-dependent crack growth model for treating oxidation-induced crack growth under small-scale creep conditions is presented in Section 2. Applications of the time-dependent crack growth model to treat the cycle-dependent and time-dependent crack growth response of ME3 are described in Section 3. Using the enhanced risk analysis tool and material constants calibrated to powder-metallurgy (PM) disk alloy ME3, the effects of grain size and tertiary γ' size on combined *time-dependent* and *cycle-dependent* crack growth in a fictitious ME3 disk is demonstrated in Section 4 for a generic rotor design and a realistic mission profile using the DARWIN. In Section 5, the results of this investigation are utilized to assess the effects of controlling grain size and tertiary γ' size on the risk of disk fracture and to identify possible means for mitigating time-dependent crack growth in hot-section components. The computational results demonstrate that controlling location-specific microstructures and properties (e.g., instigating coarse grains and coarse tertiary γ' in the rim) can be an effective means of enhancing disk life and reducing fracture risk.

2. Development of oxidation-induced crack growth model with crack-tip stress relaxation

The effects of crack-tip stress relaxation on the time-dependent crack growth rate, da/dt, response equation was investigated by considering the fracture process of the crack-tip oxide layer with and without stress relaxation at the crack tip, as shown in Fig. 1. It is envisioned that stress relaxation at the crack tip can be described in term of the transient creep, $C(t)$, field [19] that is embedded inside the K-field. For transient creep, the near-tip stresses in the y-direction normal to the crack is given by [19].

$$\sigma_{yy} = \left[\frac{C(t)}{I_n A r}\right]^{1/(n+1)} \quad (7)$$

where n is the creep exponent, $C(t)$ is the time-dependent energy integral, I_n is a normalization parameter, A is the power-law creep coefficient, and r is distance ahead of the crack tip. The corresponding stresses in the K-field are given by [20]

$$\sigma_{yy} = \frac{K}{\sqrt{2\pi r}} \quad (8)$$

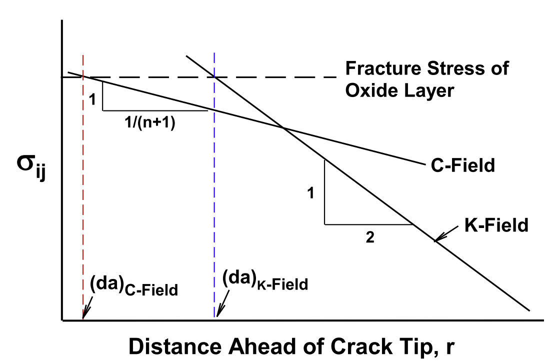

Fig. 1. Schematics of the oxide fracture process in the C-field compared to oxide fracture in the K-field. Stress relaxation at the crack tip reduces the da/dt response because the relaxed stress field is less likely to cause oxide fracture at the crack tip by decreasing the region where the critical stress for oxide fracture can be attained.

which are relaxed by transient creep near the crack tip. Instead of focusing on the critical plastic or creep strain within the crack tip element, it is more instructive and convenient to consider the fracture stress of the oxide layer formed ahead of the crack tip. For fracture of the oxide layer at a critical stress of σ_{ox}^*, stress relaxation at the crack tip would delay of onset of crack growth and reduce the amount of crack extension compared to those of the K-field without stress relaxation, as shown in Fig. 1.

For a time increment of dt, the crack increment where the oxide fracture stress is met in the C-field is r_C while the corresponding plastic zone size in the K-field is r_K. From Fig. 1, it is apparent that r_C is smaller than r_K for small-scale creep conditions. For a time increment of Δt, the crack advance in a creep-relaxed stress field is r_C compared to r_K in the K-field. As a result, the time-dependent crack growth rate, da/dt, corresponding to the relaxed crack-tip stress field is lower than that of the K-field without stress–relaxation. From Eq. (7), the creep zone that satisfies a critical oxide fracture stress is given by

$$r_C = \frac{C(t)}{I_n A \sigma_{ox}^{n+1}} \tag{9}$$

and

$$r_K = \frac{K^2}{2\pi\sigma_{ox}^2} \tag{10}$$

for the damage zone in the K-field. Dividing Eq. (9) by Eq. (10) leads one to

$$\frac{r_C}{r_K} = \frac{2\pi(1-\nu^2)}{(n+1)I_n A \sigma_{ox}^n t}\left(\frac{\sigma_{ox}}{E}\right) \tag{11}$$

after invoking [19]

$$C(t) = \frac{(1-\nu^2)K^2}{(n+1)Et} \tag{12}$$

for small-scale creep conditions, where n is the power-law creep exponent, ν is Poisson's ratio, E is Young's modulus and t is time of creep. Stress relaxation in Ni-base superalloys such as Rene 104 (ME3) and the NASA developed LSHR alloy have been shown to depend on the tertiary gamma prime (γ') size [21], as shown in Fig. 2, which in turn affects the time-dependent crack growth life. To describe the near-tip stress relaxation, the creep response within the crack-tip creep zone is considered to be governed by a power-law given by [22]

$$\dot{\varepsilon}_C = A\sigma^n \tag{13}$$

with

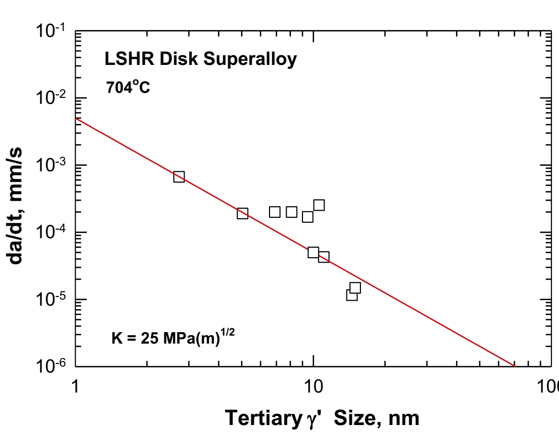

Fig. 2. Dependence of the time-dependent crack growth rate, da/dt, of a LSHR disk superalloy on the tertiary gamma prime size. Experimental data are from Telesman et al. [21].

$$A = A_o\left(\frac{b}{\lambda}\right)^q \tag{14}$$

where A_o and q are empirical constants describing the power-law creep response as a function of tertiary γ' size, b is the magnitude of the Burgers vector for slip shearing the γ', and λ is the tertiary γ' size. By matching the C-field and the K-field at the critical stress level for oxide fracture, the crack growth rate, $(da/dt)_{\text{C-field}}$, for the stress–relaxed condition can be expressed in the terms of the crack growth rate, $(da/dt)_{\text{K-field}}$, for the unrelaxed condition. The corresponding relation is given by,

$$\frac{(da/dt)_{C-field}}{(da/dt)_{K-filed}} = \frac{r_C/dt}{r_K/dt} = \frac{r_C}{r_K} \tag{15}$$

which may be combined with Eqs. 11–14 by incorporating the tertiary γ' size explicitly through the power-law creep to obtain an explicit relation between $(da/dt)_{\text{C-field}}$ and $(da/dt)_{\text{K-field}}$, leading to

$$\left(\frac{da}{dt}\right)_{C-Field} = \frac{\alpha_n^{n+1}(1-\nu^2)}{(n+1)I_n}\left[\frac{\varepsilon_{ox}^f}{\varepsilon_C}\right]\left[\frac{b}{\lambda}\right]^p\left(\frac{da}{dt}\right)_{K-Field} \tag{16}$$

where α_n is the creep coefficient, and I_n is the normalization parameter in the C-field, which is identical to that in the HRR field [23,24]. The parameter ε_c is the creep strain accumulated during stress relaxation, and ε_{ox}^f is the fracture strain of the oxide layer, and $p = 1/q$. The $(da/dt)_{\text{K-field}}$ term in the right-hand-side of Eq. (16) is given in Eqs. (5) and (6). Combining Eqs. (5) and (6) with Eq. (16) leads one to

$$\left(\frac{da}{dt}\right)_{C-Field} = B_o^C \exp\left(-\frac{Q}{RT}\right)K^m \quad \text{with } m > 0 \text{ and } K > K_{th} \tag{17}$$

and

$$B_o^C = \frac{\alpha_n^{n+1}(1-\nu^2)}{(n+1)I_n}\left[\frac{\varepsilon_{ox}^f}{\varepsilon_C}\right]\left[\frac{b}{\lambda}\right]^p\left(\frac{s_o}{t_o}\right)\left(\frac{\pi E}{2\sigma_y\varepsilon_f^*}\right)^{m/2}\left(\frac{1}{E\sqrt{\pi d_o}}\right)^m\left(\frac{D_o}{D}\right)^{m\gamma/2} \tag{18}$$

Thus, the TDCG equation for oxidation-induced crack growth with stress relaxation at the crack tip is still governed by a power-law of K, but the B_o coefficient, which is now denoted as B_o^C, is reduced as the result of stress relaxation and small-scale creep in the near-tip C-field. Furthermore, B_o^C is a function of two scaling parameters, the grain size and the tertiary γ' size. In particular, B_o^C and da/dt both decrease with increasing grain size and tertiary γ' size. For a material with a relatively constant average grain size, Eq. (18) can be recast into a scaling law expressed in terms of the tertiary gamma prime size alone, leading to

$$\left(\frac{da}{dt}\right)_{C-Field} = \left[\frac{\lambda_o}{\lambda}\right]^p\left(\frac{da}{dt}\right)_{K-Field} \tag{19}$$

with $\lambda_o \geqslant \lambda$ and

$$\lambda_o = \frac{\alpha_n^{n+1}(1-\nu^2)}{(n+1)I_n}\left[\frac{\varepsilon_{ox}^f}{\varepsilon_C}\right]^{1/p} b \tag{20}$$

For illustration purposes, the n value of power-law creep is ≈ 4, then $I_n = 5$, and $\alpha_n = 1$. Substituting these values into Eq. (20) leads one to

$$\lambda_o = \frac{b}{5}\left[\frac{\varepsilon_C}{\varepsilon_{ox}^f}\right]^p \tag{21}$$

which indicates that λ_o depends mostly on the ratio of the critical creep strain to the oxide strain at fracture for a given creep exponent n. Scaling laws for da/dN and da/dt have been developed for grain size, while a scaling law of da/dt in terms of tertiary γ' size is not necessary since the tertiary γ' size has been found to exert no influence on the da/dN response [21].

3. Model applications to ME3 disk alloy

The microstructure-based TDCG model has been applied to predict the dwell fatigue crack growth behavior of ME3, which is an advanced powder metallurgy (PM) Ni-based alloy developed in a NASA program by GE and Pratt and Whitney [25]; ME3 is now referred to as Rene 104. This alloy was chosen for this modeling effort because of the existence of a relatively large database of microstructural data [26] and mechanical properties [25] in the public domain in the form of technical reports [25–27] and paper [28]. The ME3 alloys were typically prepared by powder metallurgy (PM) methods and subsequently forged into pancakes. The forgings were then given a series of heat-treatments at subsolvus or supersolvus temperatures to produce a variety of fine-grained microstructures containing primary, secondary, and tertiary gamma prime (γ') precipitates of various sizes on the order of 1 μm or less. Fig. 3 presents a plot of tertiary γ' size versus grain size for ME3 based on published data in the literature [26–28]. The ME3 materials tested by Gabb et al. [26] and Evans [27] were of similar grain size and tertiary γ' size; both were NASA-processed materials [26]. The ME3 materials studied by Dahal et al. [28], which were from an AFRL MAI program, exhibited a larger grain size and tertiary γ' size compared to those of Gabb et al. [26] and Evans [27].

Cycle-dependent crack growth is typically described in terms of the Paris power-law equation as given by Eq. (3). Appropriate material constants in the Paris Power-Law equation were obtained for ME3 as a function of temperature and they are summarized in Table 1. Fig. 4(a) shows the fit of Eq. (3) to the da/dN data at a stress ratio, R_σ, of 0.5 for ME3 reported by Gabb et al. [25]. The stress ratio is denoted as R_σ to differentiate it from the universal gas constant, R. Time-dependent crack growth is also described in terms of a power-law equation as given by Eq. (4). For ME3, material constants are as follow: $B_o = 1.116\text{E}+5$ mm/s, $Q = 316.36$ kJ/mol K, $m = 5.388$, and $K_{th} = 19.2$ MPa$\sqrt{\text{m}}$. Fig. 4(b) shows the fit of Eq. (15) to the da/dt data at $R_\sigma = 0$ for ME3 reported by Gabb et al. [25]. The Arrhenius-law was also used to compute the da/dt response at 538 °C.

The effect of tertiary γ' size on the da/dt response was examined by applying the γ' scaling equation, Eq. (21), to the da/dt data reported by Gabb et al. [25] and Dahal et al. [28] for 704 °C. The tertiary γ' size for the ME3 material studied by Gabb et al. [25,26] was ≈ 20–33 nm, while those of Dahal et al. [28] was 42–60 nm.

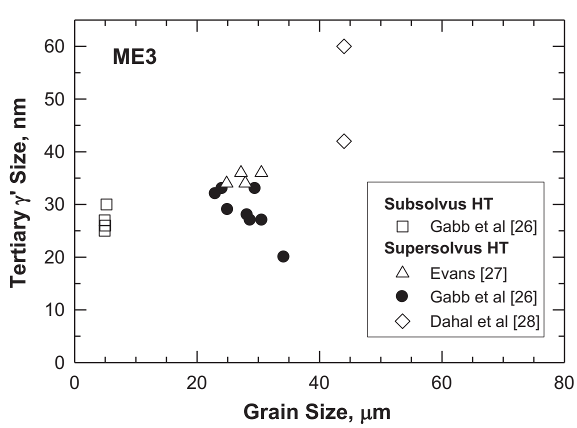

Fig. 3. A summary plot of tertiary γ' size versus grain size in ME3 for subsolvus and supersolvus heat treatments (HT). Data are from Gabb et al. [26], Evans [27], and Dahal et al. [28].

Table 1
Summary of A and n values in the Paris power-law equation for ME3 at various temperatures and R_σ ratios.

T, °C	R	A, mm/cycle/(MPa$\sqrt{\text{m}}$)^n	n	ΔK_{th}, MPa(m)$^{1/2}$
204	0.5	2.13E−10	4.157	10.4
427	0.5	5.49E−09	3.39	9.79
537	0.5	9.15E−09	3.402	10.7
649	0.5	2.41E−08	3.328	9.9
704	0.5	1.67E−08	3.669	9
21	−0.25	1.02E−12	4.903	23.8
204	−0.25	1.14E−10	3.784	23.8
427	−0.25	7.36E−10	3.416	25.2
537	−0.25	4.37E−10	3.665	N.A.
649	−0.25	4.25E−09	3.169	N.A.

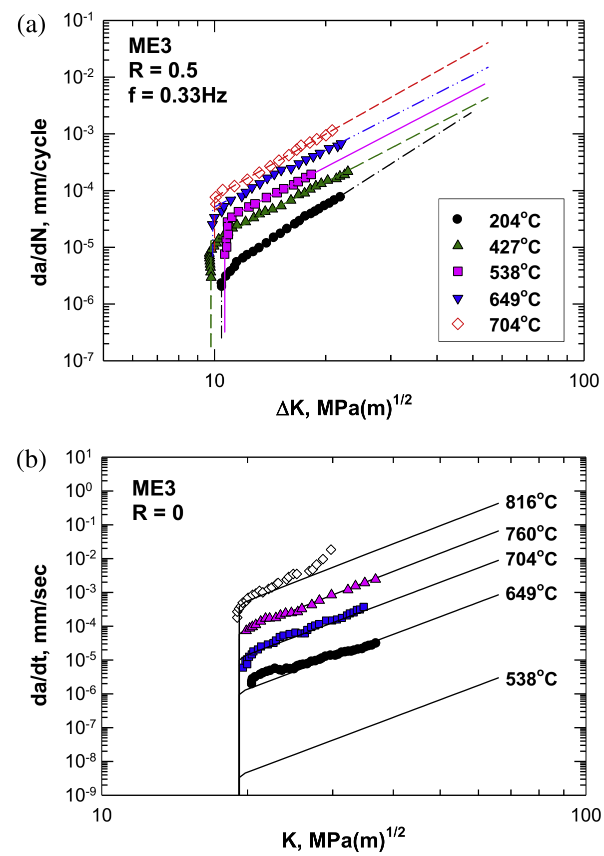

Fig. 4. Comparisons of model simulations and experimental data of fatigue crack growth rate, da/dN, and time-dependent crack growth rate, da/dt, of NASA ME3 materials (28.6 μm grain size and 28 nm tertiary γ' size) [25,26]: (a) da/dN versus ΔK, and (b) da/dt versus K at various temperatures. Experimental data were used to obtain the model constants.

The two sets of da/dt data were utilized to determine the p value based on a reference γ' size, λ_o, of 1 nm and a p value of 5 was obtained, as shown in Fig. 5.

Eq. (2) was utilized to compute the da/dN response of ME3 as a function of frequency for $\Delta K = 16.5$ MPa(m)$^{1/2}$ at $R_\sigma = 0.5$. For these computation, $dt/dN = 1/f + t_d$, where f is the frequency and t_d is the hold time at dwell. Fig. 6 shows the fatigue crack growth rates as a function of frequency for various temperatures. At high temperatures, da/dN increases with decreasing frequencies. The frequency effect diminishes with decreasing temperatures. In particular, da/dN is entirely controlled by cycle-dependent crack growth and is independent of frequency at temperatures below 204 °C, as shown in Fig. 6(a) for the NASA ME3 materials with a grain size of 27.9 μm (±3.72 μm) and a tertiary γ' size of 28.6 nm (±4.3 nm).

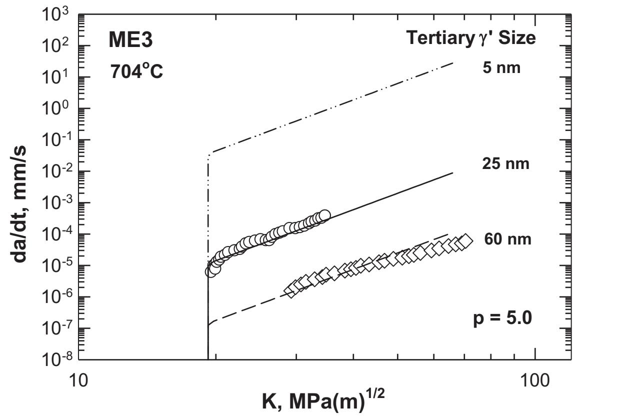

Fig. 5. Time-dependent crack growth rate of ME3 as a function of stress intensity factor, K, at 704 °C for various tertiary γ' sizes. The calculated curves are computed using the γ' size scaling law fitted to the experimental data of Gabb et al. [25,26] and Dahal et al. [28].

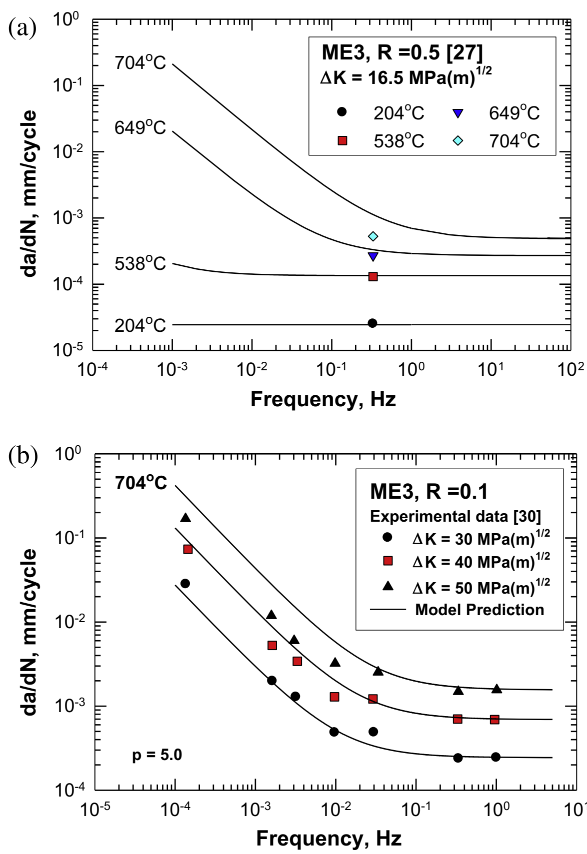

Fig. 6. Predicted da/dN response compared to measured data as a function of frequency for ME3: (a) NASA ME3 at various temperatures [25], (b) MAI ME3 at various ΔK levels at 704 °C [28].

The same approach, Eq. (2), was utilized to predict the dwell fatigue da/dN response of ME3 from the MAI program (44 μm grain size and 42–60 nm tertiary γ' size) by applying the γ' size scaling law, Eq. (19), to obtain the da/dt response. Tertiary γ' scaling was applied to the da/dt response only because the fatigue crack growth rate, da/dN, was reported to be independent of tertiary γ' size [21]. Fig. 6(b) presents a comparison of the predicted and measured da/dN response as a function of frequency for ME3 at three ΔK levels at $R_\sigma = 0.1$ for 704 °C. The comparison indicates that the agreement between model prediction and experimental is excellent for ΔK levels of 30 and 40 MPa(m)$^{1/2}$. In contrast, the model over-predicted the da/dN response at low frequency for $\Delta K = 50$ MPa(m)$^{1/2}$.

The influence of frequency and hold time during dwell fatigue on da/dN response can be quantified in terms of a dwell fatigue ratio, DFR, defined on the basis of Eq. (2). In particular, the dwell fatigue ratio can be defined as the ratio of da/dN response during dwell fatigue (DF) to the da/dN response under pure fatigue (F). Thus,

$$\mathrm{DFR} = \frac{(da/dN)_{\mathrm{DF}}}{(da/dN)_F} = \left[\frac{1}{f} + t_d\right] \frac{da/dt}{(da/dN)_F} \tag{22}$$

which can be elucidated further by combining with Eqs. (3) and (4) to give

$$\mathrm{DFR} = \left[\frac{1}{f} + t_d\right] \left[\frac{B_o \exp(-Q/RT)}{A(1-R_\sigma)^n}\right] K^{m-n} \tag{23}$$

which indicates DFR depends on the $(1/f + t_d)$ term, the ratio of B_o/A, n, and m at a given temperature T and stress ratio R_σ. Fig. 7 shows a comparison of the computed and measured DFR for ME3 materials at 704 °C and an R_σ ratio of 0.1. The compiled dataset in Fig. 7 indicates that the DFR increases with decreasing effective frequency and is essentially independent of the ΔK level. The material parameters that contribute to the B_o/A ratio appear to be a constant and is independent of the ΔK level because n and m are almost equal. The finding suggests that the large increase in the da/dN rates observed during dwell fatigue at a given temperature may originate from the exponential term, exp $(-Q/RT)$, in the da/dt response equation (Eqs. (4) and (5), or Eq. (17)) and a relatively large hold time at the peak load during dwell.

4. Life-prediction and risk assessment of a turboengine disk

In this section, life-prediction and risk assessment of a fictitious ME3 disk subjected to a realistic mission profile is presented. The objectives of this analysis are (1): to check the microstructural scaling module implemented in DARWIN, (2) to evaluate the benefits of controlling grain size and tertiary γ' size on delaying time-dependent crack growth and improving crack growth life, and (3) to assess the risk of disk failure due to grain size and tertiary γ' size variations. The demonstration problem consists of the following major components:

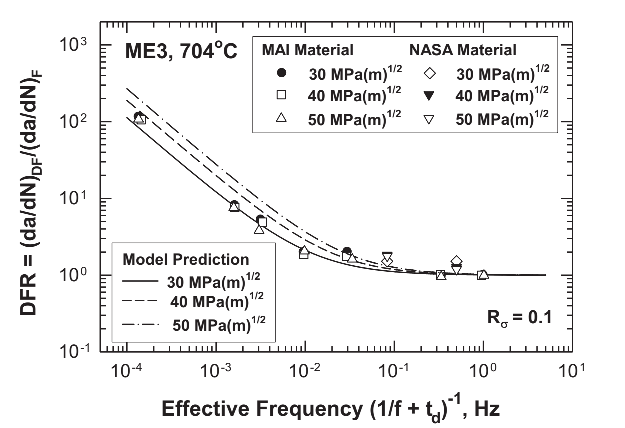

Fig. 7. Dwell fatigue ratio, which is defined as the ratio of $(da/dN)_{\mathrm{DF}}$ normalized by $(da/dN)_F$, as a function of the effective frequency for various ΔK levels at a stress ratio, R_σ, of 0.1. Experimental data are from Gabb et al. [25], Evans [27], and Dahal et al. [28].

- The material properties of an advanced powder-metallurgy (PM) disk alloy defining the constants used in the time-dependent crack growth equations implemented in DARWIN.
- Generic, non-proprietary axisymmetric rotor geometry definition of realistic complexity and size.
- Stress and temperature load step definitions for a selected gas turbine rotor disk geometry with associated mission profile and load step durations.

The PM disk alloy ME3 was selected for the DARWIN demonstration because of a set of da/dN and da/dt properties as well as the corresponding microstructural information is available in the open literature. Both the set of mechanical and microstructural properties and the corresponding life-prediction results can be shared with other OEMs. As indicated in Section 3, the mechanical and microstructural properties of the ME3 alloys utilized in this demonstration were from the a NASA program [25] and from an AFRL MAI program [28]. Both materials received a series of heat-treatments at supersolvus and/or subsolvus temperatures to produce fine-grain microstructures with a range of precipitate sizes for primary, secondary, and tertiary γ' precipitates.

The finite-element (FE) model of a fictitious rotor design selected for this demonstration problem is shown in Fig. 8. The disk was divided into three regions: (1) Region A with a uniform grain size a_i, (2) a transition region with mixed grains of sizes a_i and b_i, and (3) Region B with a uniform grain size b_i. In the transition region, the grain size varies linearly from a_i at the Region A boundary to b_i at the Region B boundary. Six cases of various grain sizes and tertiary γ' sizes were considered in the benchmark calculations. As summarized in Table 2, uniform grain size and tertiary γ' size through the disk was considered in Case 1. Fig. 9 shows the uniform grain size and tertiary γ' size within the disk as well as the location of the anomaly (crack). In Cases 2, 4 and 6, the grain size in Region A, the transition zone and Region B were varied while holding the tertiary γ' size constant. In Cases 3 and 5, the tertiary γ' size was varied in Region A, the transition zone, and Region B while the grain size was held constant.

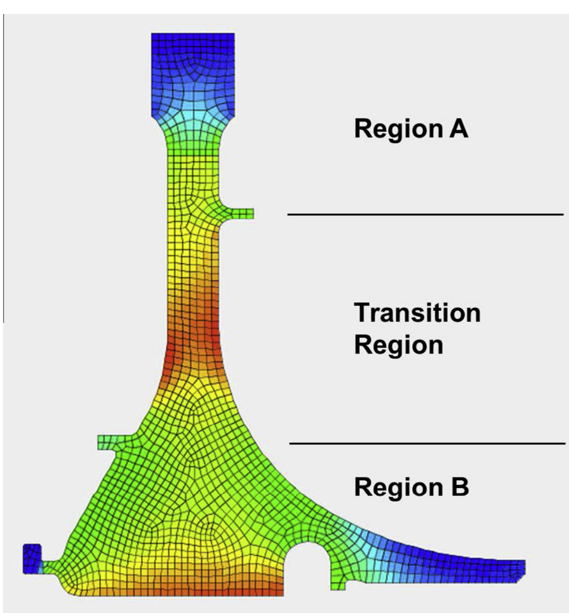

Fig. 8. The FEM mesh of a fictitious ME3 disk comprised of a Region A with a uniform grain size, a_i, a transition region of mixed grain sizes a_i and b_i, and a Region B of grain size b_i. The tertiary γ' sizes are also varied in individual regions. The color contours show regions of high stresses (red) and low stresses (blue). (For interpretation of the references to colour in this figure legend, the reader is referred to the web version of this article.)

Table 2
A summary of grain size and tertiary γ' size utilized in the life-prediction and reliability analysis of a ME3 disk with controlled (assumed) microstructure sizes.

Condition	Region A		Transition region		Region B	
	Grain size, μm	Tertiary γ' size, nm	Grain size, μm	Tertiary γ' size, nm	Grain size, μm	Tertiary γ' size, nm
Case 1	28	28	28	28	28	28
Case 2	28	28	5–28	28	5	28
Case 3	28	28	28	28–60	28	5
Case 4	5	28	5–28	28	28	28
Case 5	28	28	28	28–60	28	60
Case 6	5	28	5–56	28	56	28

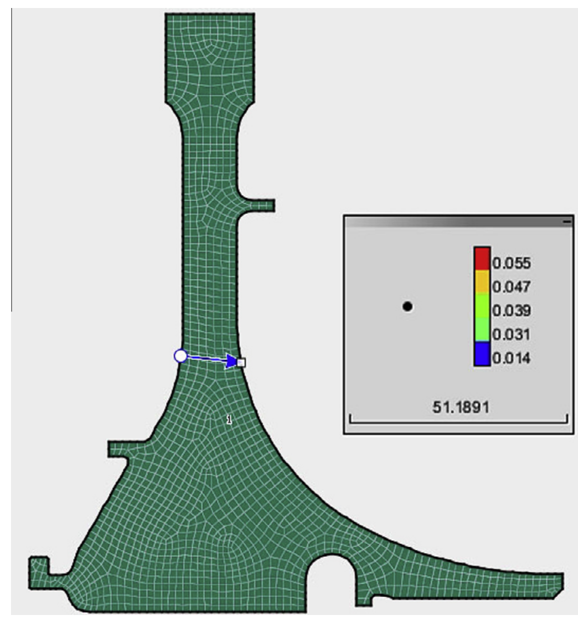

Fig. 9. ME3 disk with uniform grain size (28 μm) and uniform tertiary γ' size (28 nm). The location of the anomaly is indicated by the open circle and the crack path is denoted by the arrow.

Fig. 10(a) and (b) present the variations of grain size and tertiary γ' size in Cases 2 and 3, respectively. Similarly, Fig. 11(a) and (b) shows the variations of grain size and tertiary γ' size in Cases 4 and 5, respectively. At the current stage of development, either the grain size or the tertiary γ' size can be varied in DARWIN, but not at the same time.

A mission profile consisting of stress and temperature as a function of time and load step durations was utilized for these calculations. This mission profile, which cannot be presented here because of proprietary reasons, contained pertinent temperature, stress, and time histories that were necessary to test the time-dependent crack growth model presented in this work. For the benchmark calculations presented in this paper, the temperature histories were applied uniformly to the disk. Under the imposed load and thermal histories, Region B experienced the highest stresses and temperatures. A surface anomaly in the form of a half-penny-shaped crack was assumed to be present near a bore, and the surface anomaly distribution is shown in Fig. 12. The median of the initial crack depth was 0.2 mm. Probabilistic crack growth analyses were performed with concurrent time-dependent crack growth and cycle-dependent fatigue crack growth. Cycle counting was performed using a rain-flow method.

Some of the results of the demonstration problem are highlighted in Figs. 13 and 14. Fig. 13 plots the value of K_{max} as a

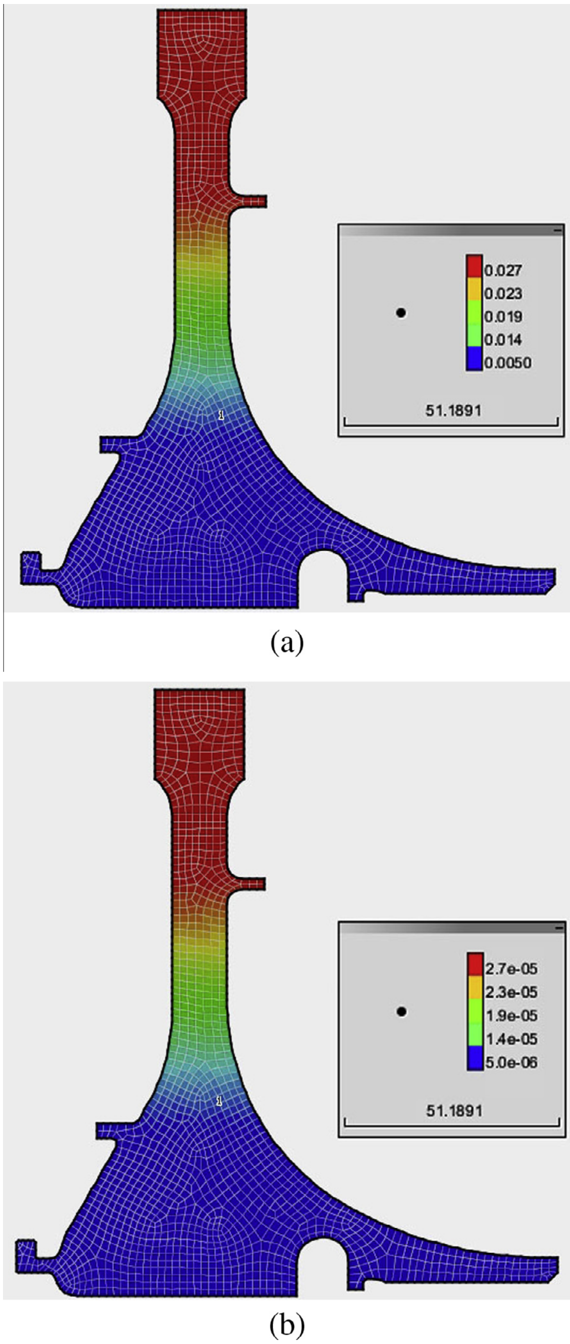

Fig. 10. Variations of microstructural feature size in the ME3 disk: (a) grain size (in mm) for Case 2, and (b) tertiary γ' size (in mm) for Case 3.

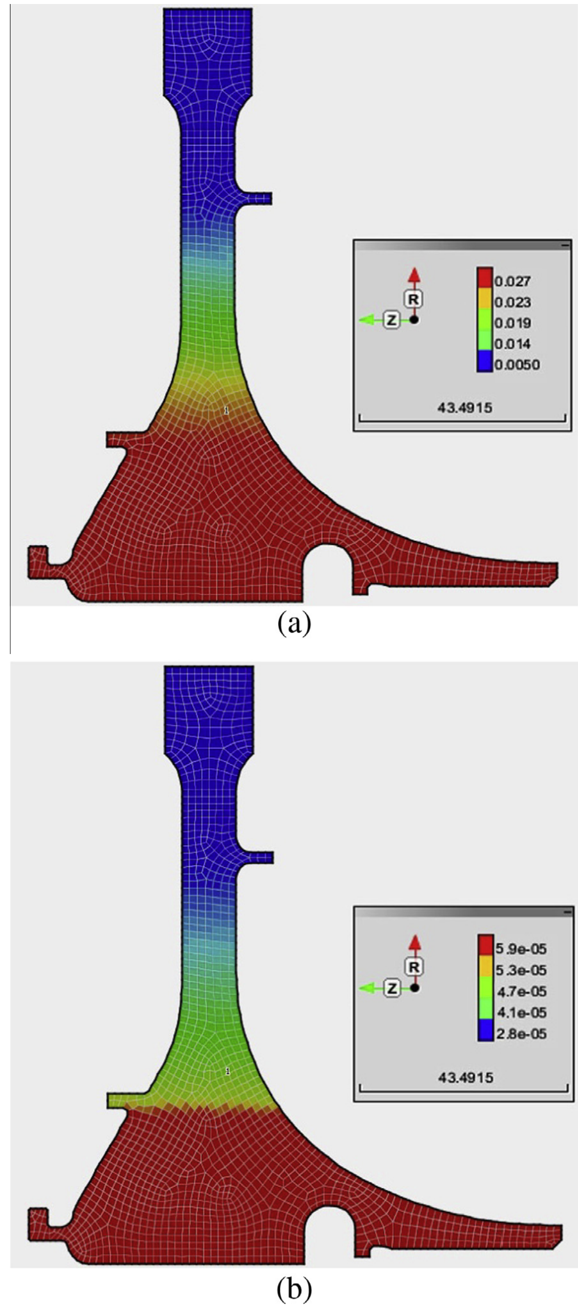

Fig. 11. Variations of microstructural feature size in the ME3 disk: (a) grain size (in mm) for Case 4, and (b) tertiary γ' size (in mm) for Case 5.

function of flight cycles, while Fig. 14 presents the corresponding cracked area as a function of flight cycles. In both figures, the actual values of K_{max} and cracked area were intentionally left out in order to protect sensitive data. Fig. 14 shows that the calculated fatigue life for ME3 disk with uniform grain size (28 μm) and tertiary γ' (28 nm) as a reference. The fatigue lives are reduced when fine grains (5 μm, Case 2) or fine tertiary γ' (5 nm) are placed in Region B. Similarly, the fatigue lives are reduced when fine grains (5 μm) are placed in Region A. In contrast, the fatigue lives are increased when coarse tertiary γ' precipitates and coarse grains (Case 5 and Case 6) are placed in Region B. These results can be understood on the basis that both cycle-dependent and time-dependent crack growth rates increase with decreasing grain size, while cycle-dependent crack growth rate is independent of tertiary γ' size and time-dependent crack growth rate decreases with increasing tertiary γ' size. These results are also complicated by the fact that the crack path is located within the transition zone, which contains a mixture of coarse and fine grains and tertiary γ' precipitates. Fig. 15 presents results of the conditional probability of fracture due to fatigue crack growth with concurrent time-dependent crack growth. As expected, the fatigue life was reduced and the risk of fracture was increased by the presence of fine grains and fine γ' precipitates in the rim region while the reverse is true when larger tertiary γ' sizes and grain sizes are placed in Region B. Thus, the time-dependent crack growth framework implemented in DARWIN appeared to work properly and successfully in this demonstration problem to illustrate the beneficial effects of controlling grain size and tertiary γ' size on improving fatigue life and reducing risk of fracture.

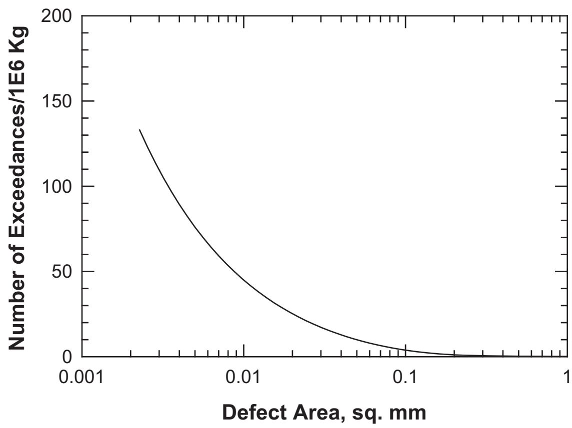

Fig. 12. Surface anomaly distribution utilized in the DARWIN demonstration problem.

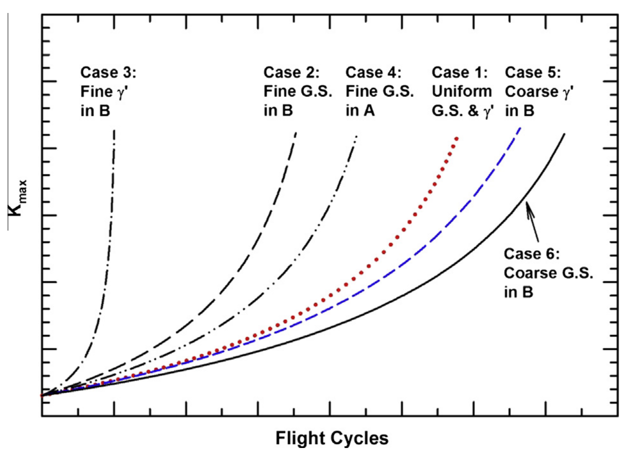

Fig. 13. DARWIN results of maximum stress intensity, K_{max}, as a function of flight cycle for the demonstration problem of this ME3 disk.

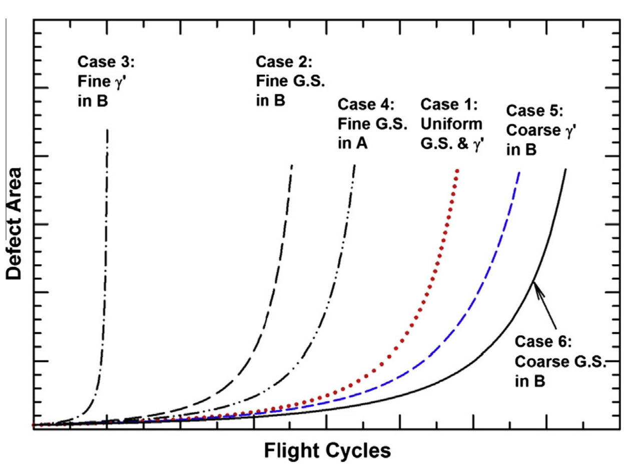

Fig. 14. DARWIN results of cracked area as a function of flight cycle for the ME3 rotor design used in the demonstration problem.

5. Discussion

One of the main assumptions utilized in the life-prediction analysis is that cycle-dependent and time-dependent crack growth can be treated via the summation law as described in Eq. (1). One of the advantages of the summation law, which has been used successfully by other investigators [7,8], is that Eq. (1) can be applied

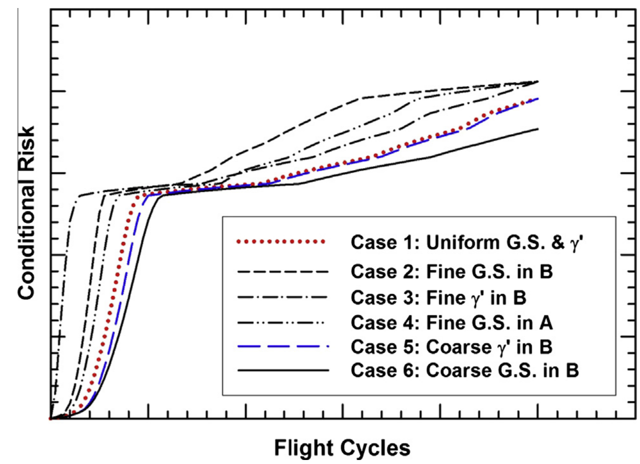

Fig. 15. Computed conditional probability of fracture as a function of flight cycle for the ME3 rotor design used in the demonstration problem.

to complex mission profiles with arbitrary stress–time and temperature–time histories simply by performing cycle-by-cycle integration of the crack growth equations according to the imposed loading and thermal histories. At a given stress and temperature, da/dN and da/dt are computed via Eqs. (3) and (4), respectively. The total crack growth increment is then summed in the manner as described in Eq. (1). Thus, there is no need to keep track of loading and unloading steps since cycle-dependent and time-dependent crack growth are taken to occur concurrently at all times with the corresponding growth kinetics governed by Eqs. (3) and (4). In addition, the dependence of da/dt on frequency is not assumed but is predicted as a natural consequence of the times spent at a given stress at an elevated temperature where the time-dependent crack growth process is operative.

It is well-known that fatigue crack growth in Ni-based superalloys usually occurs along a transgranular path, while time-dependent crack growth proceeds along the grain boundaries. The area fractions of transgranular and intergranular facets on the fracture surfaces represent the relative extents of the cycle-dependent and time-dependent fracture processes. The frequency at which cycle-dependent crack growth transitions to time-dependent crack growth can be predicted from Eq. (1) but it requires one to specific a particular percentage of intergranular facets on the fracture surfaces. Such computations have not been performed since they are not the focus of this work. In general, the transition frequency is expected to increase with increasing temperatures as less time is required to cover a given percentage of intergranular fracture area by time-dependent crack growth as the temperature increases.

Another important assumption in the disk analysis is that the stresses in the disk are nominally elastic. Any plastic flow, creep, and oxidation damages are constrained within the K-field so that the stress intensity factor (K) and its range (ΔK) are the pertinent parameters for characterizing the crack driving force. For the disk calculations considered, the mesh was sufficiently fine and the stresses are almost entirely elastic except at certain stress concentration sites. As a result, the mesh size was not an issue and mesh sensitivity was not investigated in this work but it was performed in a previous investigation [29]. The initial defect was taken to be a semi-circular crack with a crack depth of 0.2 mm. The crack was allowed to change shape as it extended in length and ultimately the 3D-crack transitioned to become a through-thickness crack. Experimental values of the yield strength of the ME3 alloy at five temperatures for the grain size of interest were provided as inputs to DARWIN. During the life-prediction computations, the yield stress value at a given temperature was obtained either directly or by interpolation from the input data. Yield strength interpolation based on grain size was not performed since such an option is not currently available in DARWIN but this capability may be added in the future.

One of the important findings of this investigation is the development of a microstructure-based time-dependent crack growth model for treating the effects of creep-induced stress relaxation at the crack tip on the crack propagation rate. The current approach on K-controlled time-dependent crack growth is motivated by previous observations that creep-induced stress relaxation at the crack tip led to retarded da/dt response [21] during dwell fatigue or long-term hold under sustained loading [30]. For a loaded crack in a creeping solid, the stresses ahead of the creep crack is known to decrease with increasing time during the transient period until steady state creep is attained. For a fracture process that obeys a critical stress failure criterion (such as oxide fracture), the da/dt response may be reduced during the transient period because the near-tip stresses decrease with increasing creep times. As the near-tip stresses approach constant during steady state, the da/dt may increase again when creep cavitation and oxidation occur concurrently along the grain boundaries. In this paper, the modeling effort is focused on the da/dt response resulting from crack-tip oxidation under the transient creep period without considering the onset of dynamic (oxygen) embrittlement or the development of creep cavities along the grain boundaries. The competition between dynamic embrittlement and oxide-induced fracture has been analyzed recently [31]. The theoretical analysis revealed that oxide formation prior to or subsequent to dynamic embrittlement would lead to essentially the same da/dt response when the transformation stress associated with the oxide formation are compressive. In both cases, the compressive transformation stresses at the crack tip must be overcome first and the subsequent da/dt is controlled by fracture of oxides formed either ahead of the crack tip or in the crack wake. The results of this investigation also demonstrated that stress relaxation at the crack tip during small-scale transient creep can significantly reduce the oxidation-induced crack growth rate by two processes: (1) limiting the crack-tip damage zone where oxide fracture can occur within the creep-relaxed stress field, and (2) preventing the near-tip stresses from reaching the critical stress for oxide fracture. Both large grain size and large tertiary γ' size retard the da/dt due to oxidation but for different reasons. A larger grain size improves da/dt resistance because diffusion of oxygen along grain boundaries decreases with increasing grain size. In comparison, da/dt resistance in ME3 is enhanced by a larger tertiary γ' size because of increasing crack-tip stress relaxation with increasing tertiary γ' sizes, which makes fracture of the oxides at the crack tip more difficult. In addition, creep-induced stress relaxation is confined to the crack tip under small-scale creep conditions such that the resulting da/dt response is entirely controlled and expressed in terms of the stress intensity factor (K) as the crack driving force. Under these circumstances, the da/dt response equation can be expressed in terms of K with the crack growth coefficient, B_o, that is a function of grain size and tertiary γ' size; this characteristic property can be utilized to develop a set of scaling laws based on the grain size and tertiary γ' size. It is also important to note that the effects of grain size and tertiary γ' size on cycle-dependent crack growth (da/dN) and time-dependent crack growth (da/dt) response can be different. For ME3, grain size scaling is applicable to both da/dN and da/dt, while tertiary γ' size scaling is applicable to da/dt only as the da/dN response is independent of the γ' tertiary size.

Evaluation of the dwell fatigue data revealed that da/dN increases with decreasing frequencies as the result of greater contributions from time-dependent crack growth due to grain boundary oxidation. Fig. 6(a) shows that the current model over-predicts the da/dN response of ME3 at 704 °C for $R_\sigma = 0.5$. The over-prediction is believed to be caused by the fact that only a small number of test data are available at several temperatures to get an accurate determination of the activation energy term, Q, in Eq. (4). It should also be noted that the da/dN response of ME3 at 704 °C shows considerably scatter but the scatter is not presented in Fig. 6(a). Another possible reason for the over-prediction is that the creep-induced stress relaxation at the crack tip may be larger than expected due to variations in the tertiary γ' size or grain size. A more extensive evaluation of the proposed model against experimental data will require additional dwell fatigue data over a wider frequency and temperature than those shown in Fig. 6(a). The over-prediction of the model for ME3 at $K = 50\ \mathrm{MPa(m)}^{1/2}$ and $R_\sigma = 0.1$ shown in Fig. 6(b) could also be attributed to increased stress relaxation due to coarsening of the tertiary γ' size and/or grain size as the time of exposure at elevated temperature (i.e., 704 °C) increases. Currently, the model does not account for the possible growth of the grain size and γ' size during high temperature exposure. Only average values of the grain size and tertiary γ' size are used to compute the da/dt response at a given temperature. Despite these simplifications, the predicted da/dt response for the dwell fatigue ratio is reasonably good even though additional improvement may still be needed at high K levels. As shown in Fig. 7, the dwell fatigue ratio (DFR), which is defined as the ratio of $(da/dN)_{\mathrm{DF}}$ to $(da/dN)_F$, increases with decreasing frequency and with increasing hold times in a dwell fatigue cycle. According to Eq. (23), DFR depends strongly on temperature and, to a lesser extent, on the material parameters that contribute to B_o, and A. On the other hand, DFR is essentially independent of ΔK, which can be explained on the basis of Eq. (23) by virtue of similar values of the crack growth exponents for da/dN and da/dt. In Fig. 7, the theoretical model over-predicted the DFR values for ME3 at high ΔK values ($\Delta K \approx 50\ \mathrm{MPa(m)}^{1/2}$) because the n and m values, which were deduced from experimental da/dN and da/dt data, were slightly different.

Before discussing the effects of grain size and tertiary γ' size on the disk life, it is important to note that this work represented the first effort to apply a microstructure-based time-dependent crack growth model in a probabilistic life-prediction analysis of an engine disk. In this analysis, the computed disk life is based on crack growth alone without considering the crack initiation life as an appropriate microstructure-based fatigue crack initiation model is not currently available. Since the effects of grain size on crack initiation life is opposite to those for crack growth life [32,33], the conclusion reached in this paper is limited to the crack growth life only and should not be applied to situations where crack initiation life is significant. When dominated by crack initiation, the disk life may be improved by a microstructure of a fine grain size as a fine-grained microstructure is more resistant to fatigue crack initiation compared to a large-grained microstructure. With the caveat of being a crack growth analysis, the DARWIN life-prediction calculations show clearly that variations in grain size and tertiary γ' size can have significant impacts on the disk life and the fracture risk. Compared to a microstructure of a uniform grain size and tertiary γ' size, coarse grains and coarse tertiary γ' in Region B are beneficial as both improve the disk life and reduce the fracture risk. The enhancement in the crack growth life is the consequence of reduced time-dependent crack growth rates (da/dt) in Region B and in the transition zone near Region B where oxidation-induced crack growth occurs. The DARWIN simulations demonstrated that the disk life can be improved by tailoring the local microstructural features such as the grain size and the tertiary γ' size. In particular, instigating coarse grain size and coarse tertiary size in Region B appears to be an effective means for mitigating time-dependent crack growth due to oxidation. In addition, the DARWIN simulations also indicate that fine grains and fine tertiary γ' in Region B and in the transition zone would have detrimental effects on disk life and increase the risk of disk fracture. Thus, it is extremely important to control grain size and tertiary γ' variations in order to prevent life debits due to the presence of the undesirable microstructural feature size at critical locations where the disk life can be impacted severely. Overall, the DARWIN simulations serve to demonstrate the potential benefits of improving disk life and reduced risk of disk fracture when location-specific microstructure and properties are taken into account when performing life-prediction and risk assessment analyses of gas turbine disks. In general, a fine grain size is beneficial for crack initiation life, while a coarse grain size is beneficial for crack growth life [32,33]. A similar trend appears to be applicable to the tertiary γ' size. Future work should, therefore, consider both crack initiation and crack growth, an effort which is currently underway.

6. Conclusions

The conclusions and achievements obtained in this investigation are as follows:

1. A microstructure-based time-dependent crack growth model has been developed for treating oxidation-induced crack growth with stress relaxation at the crack tip for small-scale creep conditions. Appropriate scaling laws for treating the effects of grain size and tertiary γ' size on da/dt have also been developed.
2. The time-dependent crack growth model has been tested and verified against experimental data of an advanced powder-metallurgy alloy ME3 for static crack growth and dwell fatigue conditions at elevated temperatures.
3. The time dependent crack growth life-prediction methodology has been integrated into the DARWIN code and illustrated by performing life-prediction and risk analyses on a fictitious disk made from an advanced powder-metallurgy disk alloy (ME3) to demonstrate the competition of multiple damage modes involving interactions of cycle-dependent crack growth and time-dependent crack growth for mission profiles that contain high heat dwell at elevated temperatures.
4. The beneficial effects of coarse grain size in the bore and in the rim of a turboengine disk have been simulated using DARWIN and the assumed grain structures in a ME3 disk.
5. The beneficial effect of coarse tertiary γ' size in mitigating time-dependent crack growth has been demonstrated by DARWIN simulation on a ME3 disk with the assumed microstructure.

Acknowledgements

This work was supported by NAVAIR under contract No. N68335-13-C-0101 and monitored by Mr. Raymond A. Pickering. The assistance by Ms. Lori Salas, SwRI, in the preparation of the manuscript is acknowledged.

References

[1] Fitch SHK, Chan KS. Life and reliability prediction for turbopropulsion systems, Phase I final report. Contract No. N68335-11-C-0171, Mustard Seed Software, Charlottesville, VA; July 2011.
[2] Fitch SHK, Chan KS. Life and reliability prediction for turbopropulsion systems, Phase I option final report. Contract No. N68335-11-C-0171-P00001, Elder Research Inc., Charlottesville, VA; July 2012.
[3] Gayda J, Gabb TP, Kantzos PT. The effect of dual microstructure heat treatment on an advanced nickel-base disk alloy. In: Green KA, Pollock TM, Harada H, Howson TE, Reed RC, Schjirra JJ, Walston S, editors. Superalloys. TMS; 2004.
[4] Gabb TP, Gayda J, Telesman J, Garg A. The effects of heat treatment and microstructure variations on disk superalloy properties at high temperature. In: Reed RC, Green KA, Caron P, Gabb TP, Fahrmann MG, Huron ES, Woodard SA, editors. Superalloys. TMS; 2008.
[5] Gabb TP, Kanzos PT, Telesman J, Gayda J, Sudbrack CK, Palsa B. Fatigue resistance of the grain size transition zone in a dual microstructure superalloy disk. Int J Fatigue 2011;33:414–26.
[6] DARWIN® User's Guide. San Antonio, TX: Southwest Research Institute; 2011.
[7] Wei RP, Landes JD. Mater Res Stand 1969;44(46):25–7.
[8] Van Stone RH, Slavik DC. In: Halford GR, Gallagher JP, editors. Fatigue and fracture mechanics, ASTM STP 1389, vol. 31. West Conshohocken, PA: ASTM; 2000. p. 405–26.
[9] Chan KS, Enright MP, Moody JP, Hocking B, Fitch SHK. J Eng Gas Turbine Power 2012;134:122501.
[10] Paris PC, Erdogan F. Trans ASME J Basic Eng Ser D 1963;85(3).
[11] Chan KS, Enright MP. ASME J Eng Gas Turbines Power 2006;128:889–95.
[12] Shahinian P, Sadananda K. J Eng Mater Tech 1979;101:225–30.
[13] Sadananda K, Shahinian P. In: Sadananda K, Rath BB, Michel DJ, editors. Micro and macro mechanics of crack growth. Warrendale, PA: Metallurgical Society of AIME; 1981. p. 119–30.
[14] Pedron JP, Pineau A. Mater Sci Eng 1982;56:143–56.
[15] Floreen S, Raj R. ASM 1983:383–404.
[16] Woodford DA. Energy Mater 2006;1(1):59–79.
[17] Chan KS, Enright MP, Moody JP, Fitch SHK. Metall Mater Transactions A; 2013 http://dx.doi.org/10.1007/S11661-013-1971-9 [published on-line].
[18] Chan KS, Enright MP, Moody JP. J Eng Gas Turbines Power 2014;136(22502):1–8.
[19] Riedel H, Rice JR. Fracture mechanics, ASTM STP 700. ASTM: Philadelphia, PA; 1980. p. 112–130.
[20] Irwin GR. ASME Trans J Appl Mech 1957;24:361–4.
[21] Telesman J, Gabb TP, Garg A, Bonacuse P, Gayda J. In: Reed RC, Green KA, Caron P, Gabb TP, Farhmann MG, Huron ES, Woodard SA, editors. Superalloy. Warrendale, PA: TMS; 2008. p. 807–16.
[22] Wu X-J, Koul AK. Metall Mater Trans A 1995;20A:905–10.
[23] Hutchinson JW. J Mech Phys Solids 1968;16:13–21.
[24] Rice JR, Rosengren GF. J Mech Phys Solids 1968;16:1–12.
[25] Gabb TP, Telesman J, Kantzoos PT, O'Connor K. Characterization of the temperature capabilities of advanced disk alloy ME3, NASA/TM-2002-211796. Cleveland, OH: NASA Glen Research Center; 2002.
[26] Gabb TP, Garg A, Ellis DL, O'Connor KM. Detailed microstructural characterization of the disk alloy ME3, NASA/TM-2004-213066. Cleveland, OH: NASA Glen Research Center; 2004.
[27] Evans JL. Environment assisted crack growth in Ni-base superalloys at elevated temperature. Ph.D. dissertation. Mechanical engineering, University of Arkansas; August 2008.
[28] Dahal J, Maciejewski K, Ghonem H. In: Reed RC, Green KA, Caron P, Gabb TP, Farhmann MG, Huron ES, Woodard SA, editors. Superalloy. Warrendale, PA: TMS; 2008. p. 807–16.
[29] Chandra R, Golden P, Enright MP, Chan KS. Fretting fatigue-based risk assessment of gas turbine engine disks. In: Paper AIAA-2008-2227, 49th AIAA structures, structural dynamics, and materials conference. AIAA, Schaumburg, IL; April 7–10, 2008.
[30] Telesman J, Gabb TP, Kantzos P. Effect of overloads on time dependent fatigue crack growth in a nickel based superalloy. In: Blom AF, editors. Fatigue 2002, proceedings of the 8th Intl Fatigue Conf, Stockholm, Sweden, vol. 5; 2002. p. 2887–94.
[31] Chan KS. A grain boundary fracture model for predicting dynamic embrittlement and oxidation-induced cracking in superalloys. Metall Mater Trans A; 2015 http://dx.doi.org/10.1007/s11661-015-2860-1 [published on-line].
[32] Chan KS. A scaling law for fatigue crack initiation in steels. Scr Metall Mater 1995;32(2):235–40.
[33] Chan KS, Enright MP. Probabilistic micromechanical modeling of fatigue life variability in an $\alpha + \beta$ Ti-alloy. Metall Mater Trans A 2005;36A:2621–31.